

Article

# Experimental Investigation of Ocean Wave Measurement Using Short-Range K-Band Radar: Dock-Based and Boat-Based Wind Wave Measurements

Jian Cui <sup>1,\*</sup>, Ralf Bachmayer <sup>1,2</sup>, Brad de Young <sup>3</sup> and Weimin Huang <sup>1</sup> <sup>1</sup> Faculty of Engineering and Applied Science, Memorial University, St. John's, NL A1B 3X5, Canada<sup>2</sup> MARUM, University of Bremen, 28359 Bremen, Germany<sup>3</sup> Department of Physics and Physical Oceanography, Memorial University, St. John's, NL A1B 3X7, Canada\* Correspondence: [jianc@mun.ca](mailto:jianc@mun.ca)

Received: 21 May 2019; Accepted: 4 July 2019; Published: 6 July 2019



**Abstract:** In this paper, an ocean wave measurement technique and a newly developed short-range K-band radar are tested. In previous work, the technique and its feasibility were studied based on numerical simulations and wave tank experiments, while its performance at sea was still unknown. Surface current, Stokes drift, and wave breaking can greatly complicate interpreting radar backscatters. The feasibility of the technique needed to be further investigated with sea experiments. Experiments were carried out at a stationary site and from a moving platform. The short-range K-band radar transmitted continuous wave and received backscatters at low-grazing angles. The Bragg-scattering from the radar's effective footprint dominated the backscatters. The Doppler shift frequency of the Bragg-scattering was attributed to the phase velocity of Bragg waves and modulated by the surface motions induced by current, Stokes drift, platform, and gravity waves. These sources of the Doppler shift frequency were analyzed, and the components induced by wind waves were successfully retrieved and converted into wave spectra that were consistent with the measurements of wave rider buoy. The experimental investigation further validated the feasibility of using short-range K-band radar to measure ocean waves.

**Keywords:** wind wave measurement; short-range K-band radar; effective footprint; Bragg-scattering; sea spikes; platform motion compensation

## 1. Introduction

Many microwave radar remote sensing techniques are available to measure ocean waves. Downward looking frequency-modulated continuous-wave (FMCW) radars measure wave height and period by measuring the vertical distance from ocean platforms or ships to sea surface. Radac's X-band WaveGuide [1] and Miros' C-band WaveFinder [2] are two commercial products that feature high measurement accuracies but suffer from the signal strength fluctuations caused by chaotic surface and the strong multiple reflections between the surface and the radar. Some techniques are based on marine navigation radars that scan the sea surface at low grazing angles and give directional spectra by analyzing a sequence of sea clutter images or Doppler images. OceanWaveS' WaMoS II [3] and ISR's CORrad [4] are two wave radar products based on X-band marine navigation radars which generate images covering sea surface of a few square kilometers. Besides the land-based or ship-borne radars, space-borne and air-borne radars, such as radar altimeter [5,6] and synthetic aperture radar (SAR) [7,8], are also used to measure ocean waves by mapping sea surface at high resolution and over large areas. Instead of distance measurements and the radar images in various types and scales, we developed a

technique using a short-range K-band radar, which focuses on the Doppler shift caused by surface motions and retrieves wave spectrum based on the relationship among the Doppler shift, wave orbital velocity and wave characteristics [9,10].

The K-band radar does not transmit pulse signals or FMCW sweep signals scanning sea surface; rather, it transmits unmodulated continuous waves (CW) at low grazing angles and receives backscatters that are shifted in frequency. The frequency shift is caused by the surface motions and referred to as Doppler shift frequency (DSF). The technique was theoretically evaluated with numerical simulations, and its feasibility was also validated in wave tank experiments under ideal conditions with regular waves [11]. In reality, ocean waves are distributed in a broad spectrum and accompanied by surface current, Stokes drift [12], and breaking events. Therefore, the experimental investigation was conducted to analyze the impact of these factors on estimating the wave spectrum.

In the experimental investigation, the concept of an effective footprint is first defined, which is a small facet of the sea surface. Backscatter from the effective footprint dominates the backscattered power and carries various DSF components that originate from Bragg waves [13,14] but are modulated by surface current, Stokes drift, platform motion, and gravity waves. Bragg waves and surface current cause constant DSF components that are proportional to the phase velocity of the Bragg waves and the velocity of the surface current, respectively. Stokes drift [15] introduces slow fluctuations of DSF when various wind waves travel through the effective footprint. Platform motion also introduces a DSF component due to the radar's velocity relative to the effective footprint. Gravity waves contribute some periodic components [16,17]. Additionally, breaking waves cause non-Bragg scattering which features large DSF components with wide bandwidth and strong power, referred to as sea spike [18,19]. According to the properties of these DSF sources, the corresponding components can be identified. The components from gravity waves remain after removing others and are converted into a wave spectrum. In this article, we analyze the DSF sources and yield wind wave measurements with the radar located on a dock and a boat.

This paper is organized as follows: Section 2 includes the definition of the radar's effective footprint, the analyses of the DSF sources, and the general processing of wave spectrum retrieval. Sections 3 and 4 describe the dock-based experiment and the boat-based experiment, respectively. Section 5 discusses the limitations and errors in the measurements, and the possible solutions. Section 6 draws some conclusions.

## 2. DSF Sources and Wave Spectrum Retrieval

### 2.1. Effective Footprint

By definition, the radar's footprint is an area illuminated by the radar beam. The total power backscattered from the Bragg waves depends on the backscatters within the K-band radar's footprint. However, the power is dominated by a portion of the footprint because the power fades quickly away from the center of the beam. The dominant portion is referred to as the effective footprint, in which the backscattered power decreases by -3 dB from the peak power. The location and dimension of the effective footprint depend on the height ( $H_a$ ) and grazing angle ( $\theta_g$ ) of the antenna. Here, two examples of effective footprints are given. With the conditions of the radar antenna and wind as shown in Table 1 and the same procedures of the numerical simulation as described in [11], the locations and dimensions of the effective footprints can be estimated.

Figure 1 shows the locations and dimensions of the two effective footprints for two different settings of  $H_a$  and  $\theta_g$ . The effective footprints are roughly elliptical, although they will slightly deform and oscillate if ocean waves pass through. A small effective footprint is preferred because the sea surface motions within it are similar. The sea surface motions in the effective footprint contribute an intensive DSF component to the Bragg-scattering. The sources of sea surface motion are introduced in the following subsections.

**Table 1.** Conditions of radar antenna and wind.

	Parameters	Notation	Value	Unit
Radar antenna	Transmission frequency	$f_T$	24	GHz
	Horizontal -3dB beam width	-	7	degree
	Vertical -3dB beam width	-	25	degree
Wind	Wind speed	$U_{10}$	8	m/s
	Wind direction	-	0 (upwind)	degree

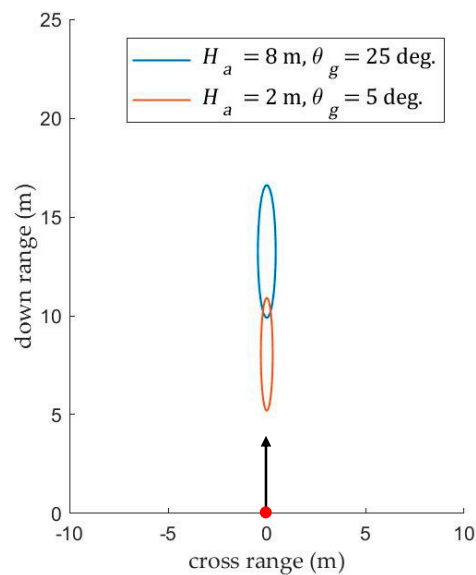


**Figure 1.** Two effective footprints. The radar is located at the red point (0, 0). The arrow points to the transmission direction. The sea surface is flat except for Bragg waves generated by an 8 m/s wind blowing towards the radar.

## 2.2. DSF Sources

### 2.2.1. Bragg Waves and Surface Current

Bragg waves cause a constant DSF that equates to Bragg frequencies [20] given by:

$$f_{b\pm} = \pm \sqrt{\frac{ng \cos(\theta_g)}{\pi \lambda}} \quad n = 1, 2, 3 \dots \quad (1)$$

where  $\lambda$  is the radar wavelength, 0.0125 m, and  $g$  is the gravitational acceleration.  $f_{b-}$  and  $f_{b+}$  are constant and originated from receding and advancing Bragg waves, respectively. The first order ( $n = 1$ ) Bragg frequency are  $-15.8$  Hz and  $15.8$  Hz if  $\theta_g$  is small. The constructive interference of electromagnetic waves backscattered from Bragg waves intensifies the power at  $f_{b-}$  and  $f_{b+}$ , which is much higher than the power backscattered from other capillary waves. Therefore, Bragg peaks are formed at  $f_{b-}$  and  $f_{b+}$  in the Doppler power spectrum of the received signals, and the first order Bragg peaks are much higher than other Bragg peaks. Furthermore, one peak is usually much higher than the other because either receding or advancing Bragg waves dominate the footprint. An example of two Bragg peaks is shown in Figure 2 and denoted by the blue curve. The right peak is higher than the left peak because the advancing Bragg waves dominate.

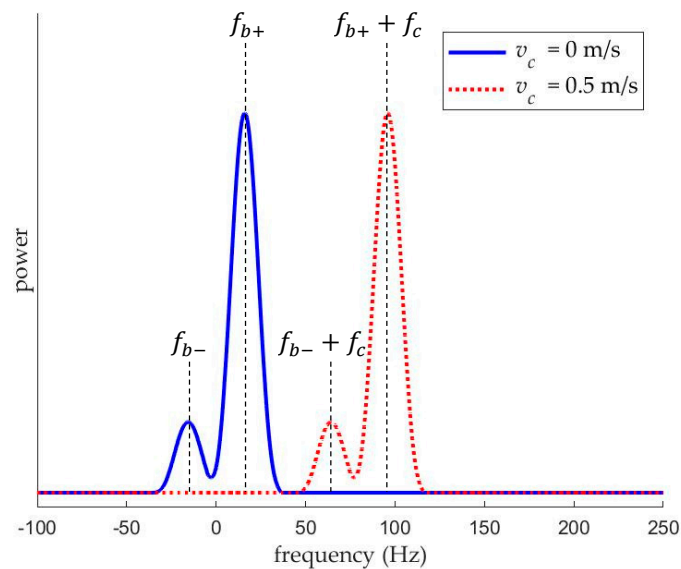


**Figure 2.** Two Bragg peaks in Doppler power spectrum. If  $v_c = 0$  m/s, two peaks present at  $-15.8$  Hz and  $15.8$  Hz for receding and advancing Bragg waves, respectively, otherwise two peaks shift along the frequency axis. Here if  $v_c = 0.5$  m/s, two peaks shift right  $80$  Hz.

The other constant component of DSF is caused by surface current because its direction and velocity in the effective footprints remain unchanged in a short time. Here, the DSF is expressed as:

$$f_c = \frac{2v_c}{\lambda} \quad (2)$$

where  $v_c$  is the relative velocity of the surface current to the antenna.  $f_c$  can cause two Bragg peaks to shift along the frequency axis in the Doppler power spectrum. An example of the shifted peaks is also shown in Figure 2 and denoted by the red dotted curve.

### 2.2.2. Stokes Drift

Wind waves are generally not sinusoidal. They have flattened troughs and sharpened crests so that the water particles no longer trace closed orbits, but undergo a slow drift in the direction of wave propagation, which is called Stokes drift. The average Stokes drift speed [15] for a deep-water wave can be estimated from:

$$v_d = a^2 \omega k e^{2kz_0} \quad (3)$$

where  $a$  is the wave amplitude,  $\omega$  is the angular frequency,  $k$  is the wave number,  $z_0$  is the average of vertical axis of water particles and equal to 0 for surface waves. Stokes drift speed causes DSF  $f_d$ :

$$f_d = \frac{2v_d \cos(\theta_g)}{\lambda} \quad (4)$$

Table 2 shows two calculation examples of Stokes drift speed and DSF for deep-water wind waves.  $T$  and  $L$  are wave period and wave length, respectively.  $L$  is estimated with dispersion relation for ocean waves [21]. In a wind wave field, the Stokes drift speed fluctuates with wind waves of different amplitudes and periods. The fluctuation of the Stokes drift speed thereby causes the fluctuation of DSF  $f_d$ .

**Table 2.** Two calculation examples of  $v_d$  and  $f_d$ .

$a$ (meter)	$T$ (second)	$L$ (meter)	$\omega$	$k$	$v_d$ (m/s)	$f_d$ (Hz)
0.20	2	6.2	3.14	1.01	0.13	20.3
0.30	3	14.0	2.09	0.45	0.08	13.5

### 2.2.3. Platform Motion

In the case of the K-band radar being mounted on a moving platform, such as a fishing boat, a container vessel, or an unmanned surface craft; usually, the radar undergoes motions in six degrees of freedom, including three rotational motions (roll, pitch, and yaw) and three linear motions (surge, sway, and heave) [22]. Figure 3 depicts the six motions. The three rotational motions alter the radar's orientation which impacts the location of the effective footprint, and they need to be mechanically compensated to keep a relatively stable effective footprint.

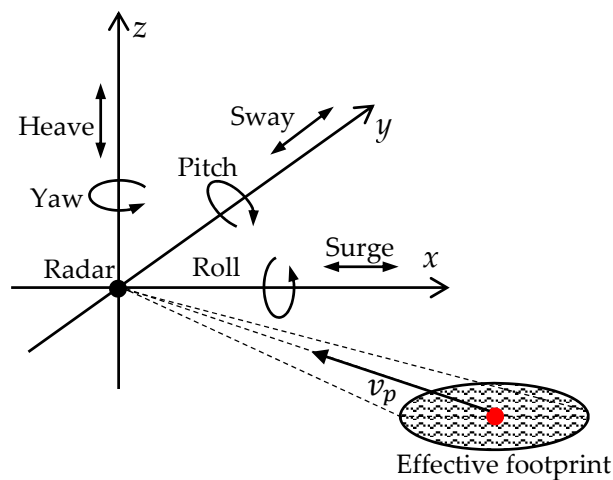


**Figure 3.** Three rotational motions and three linear motions of the K-band radar. The right-hand coordinate system  $xyz$  is built with the origin at the radar. The  $x$ -axis is parallel to the mean sea surface and follows the radar direction. Roll, pitch and yaw are rotational motions around  $x$ ,  $y$ , and  $z$ -axes, respectively; surge, sway, and heave are linear motions along  $x$ ,  $y$ , and  $z$ -axes, respectively. The center of the effective footprint is marked with the red point.

Three linear motions cannot be mechanically compensated. They cause an extra component ( $v_p$ ) to the radar's velocity relative to the effective footprint. If the three linear motions are recorded and the average location of the center of the effective footprint is estimated, the relative velocity component  $v_p$  is then determined, and the resultant DSF component is:

$$f_p = \frac{2v_p}{\lambda} \quad (5)$$

The linear motions also cause a slight shift of the location of the effective footprint. The slight shift does not change the Bragg waves, surface current, and Stoke drift. When the wavelengths of wind waves are much longer than the slight shift, the DSF deviation caused by the shift is much smaller than the amplitude of the DSF. Therefore, the shift has a negligible impact on the measurement.

### 2.2.4. Surface Gravity Wave

The DSF component generated by wave orbital motions is introduced in our previous research [11]. It is determined from the height ( $H$ ) and period ( $T$ ) of the wave:

$$f_w = \frac{2\pi H}{\lambda T} \left[ \frac{\cosh k(d+z_0)}{\sinh kd} \right] \cos\left(kx_0 - \frac{2\pi}{T}t - \theta_g\right) \quad (6)$$

where  $k$  is wave number,  $d$  is the water depth, and  $(x_0, z_0)$  is the mean position of the wave orbital motion. Here  $(x_0, z_0)$  can be set at the center of the effective footprint if the wave is long enough to cause nearly identical orbital motions in it. When many ocean waves simultaneously travel through the effective footprint, each wave independently generates a DSF component and  $f_w$  become a linear combination of them. In other words, each component in the wave spectrum has a corresponding component in the spectrum of  $f_w$  and vice versa. Consequently, the wave spectrum can be retrieved from the spectrum of  $f_w$ .

A short-range K-band radar can directly measure the total DSF of Bragg-scattering, denoted by  $f_\Sigma$ , which is originated from Bragg waves but independently modulated by the surface current, Stokes drift, platform motion, and surface gravity waves. Therefore, the total DSF of Bragg-scattering becomes:

$$f_\Sigma = f_{b\pm} + f_c + f_d + f_p + f_w \quad (7)$$

$f_{b\pm}$  and  $f_c$  are constants and can be removed by subtracting the mean value of  $f_\Sigma$ .  $f_d$  can be extracted and removed as slow fluctuations.  $f_p$  is measurable and removable if the linear motions of the platform are recorded. The only remaining DSF is  $f_w$ .

### 2.3. Wave Spectrum Retrieval

The short-range K-band radar receives the backscatters from sea surface and outputs an intermediate frequency (IF) signals which contain the DSF from the sources as discussed in the Section 2.2. The spectra of the ocean waves can be obtained by processing the IF signals as shown in flow chart in Figure 4.

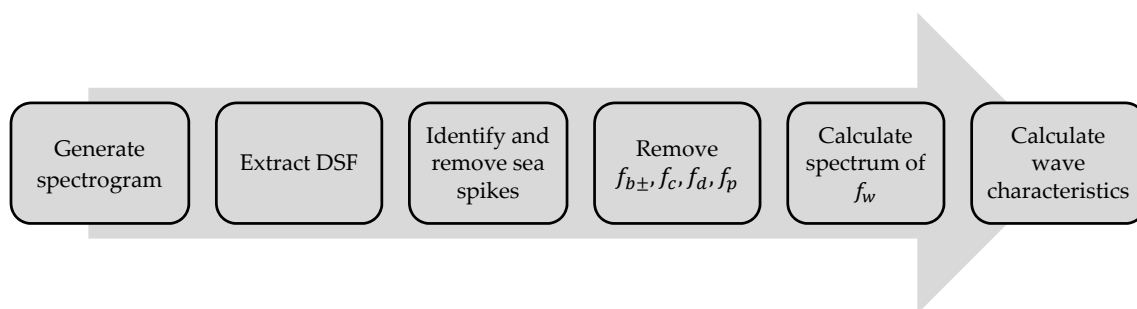


**Figure 4.** Processing flow for the IF output of the K-band radar. DSF: Doppler shift frequency.

The interpretation of each step in the processing is to

- (1) Generate the spectrogram: the time series of IF signals are transformed into the frequency domain using the short-time Fourier transform (STFT). The results are arranged into a time-frequency-power spectrogram in which the strong backscatters and the DSF become visible.
- (2) Extract DSF: the frequency at the maximum power of each instant in the spectrogram is extracted.
- (3) Identify and remove sea spikes: sea spikes have wide bandwidths and strong power in the spectrogram. They need to be identified and removed because they are neither generated by Bragg-scattering nor a source of DSF in  $f_\Sigma$ . By removing sea spikes, the remaining time series of DSF is  $f_\Sigma$ , which is caused by the motions of the Bragg waves within the effective footprint.

- (4) Remove  $f_{b\pm}$ ,  $f_c$ ,  $f_d$ ,  $f_p$ : these DSF components are removed according to the properties of Bragg waves, surface current, Stokes drift, and platform motions. The remaining component is  $f_w$ .
- (5) Calculate spectrum of  $f_w$ : an amplitude spectrum is obtained from the time series of  $f_w$  by applying discrete Fourier transform [23]. The amplitude spectrum is then converted into a wave height spectrum. Suppose  $A_i$  is the  $i$ th component of the amplitude spectrum, then the  $i$ th component ( $H_i$ ) of the wave height spectrum [11] can be calculated with:

$$H_i = \frac{A_i \lambda T}{2\pi} \left[ \frac{\text{SINH } kd}{\text{COSH } k(d + z_0)} \right] \quad (8)$$

The wave spectral density  $S_{wave}(f)$  is determined by the wave height spectrum as:

$$S_{wave}(f) = \frac{H(f)^2}{2} \quad (9)$$

- (6) Calculate wave characteristics: significant wave height, mean spectral period of ocean waves are calculated from the wave spectral density  $S_{wave}(f)$  [24].

$$H_s = 4 \sqrt{M_0} \quad (10)$$

$$T_z = \sqrt{\frac{M_0}{M_2}} \quad (11)$$

where  $M_n$  is the  $n$ th spectral moment:

$$M_n = \int_0^{\infty} f^n S_{wave}(f) df, \quad \text{for } n = 0, 1, 2, \dots \quad (12)$$

In the experimental investigation, we tried to measure the spectra and characteristics of wind waves which were generated by local prevailing wind and traveled in the wind direction. The periods of wind waves were much less than 10 s, and the breaking events frequently occurred on the crests of the wind waves. Dock-based and boat-based experiments were carried out. Two experiments are introduced and discussed in the next two sections.

### 3. Dock-based Experiment

#### 3.1. Conditions and Setup

The dock-based experiment was carried out on the dock located at the southern end of the eastern side of Conception Bay of Newfoundland, Canada, and affiliated to the Holyrood Thermal Generating Station. The dock height was 6 meters above the sea surface. The water depth was about 14 meters. There was a TRIAXYS Wave Buoy deployed near the dock. A wind sensor was mounted on the buoy about 2 meters above the sea surface to measure the wind direction and speed ( $U_2$ ) which was averaged over a 30-min. period. The average wind speed  $U_{10}$  was converted from  $U_2$  with the relationship between the average wind speeds at two different heights as described in [25].

Figure 5a shows the bird-view of the dock. The red dot indicates the radar location on the dock. The radar has a short-range K-band transceiver (K-MC3) made by RFbeam Microwave GmbH in St. Gallen, Switzerland, and its beam widths are 7 degrees in azimuth and 25 degrees in elevation. The radar's settings as well as the wind and wave conditions are listed in Table 3. The wind blew steadily over the sea surface and created wind waves, which propagated in the wind direction. The radar transmitted against the wind waves. Figure 5b shows the sea state observed along the radar beam, in which the wind waves were propagating towards the radar and some breaking events were

occurring at the wave crests in different scales. The green ellipse roughly outlines the effective footprint in the size of the blue ellipse in Figure 1.

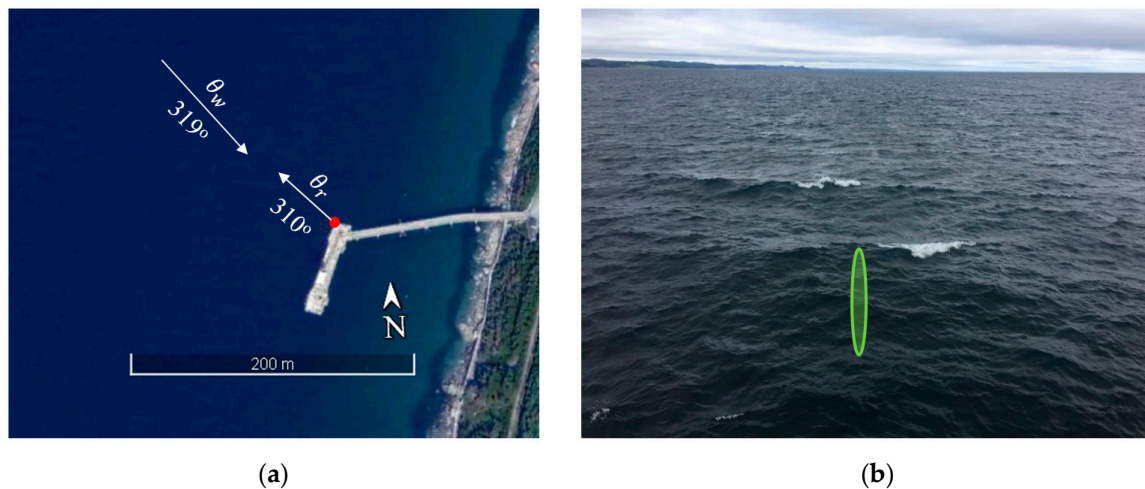


**Figure 5.** (a) Bird view of the dock (from Google Maps).  $\theta_w$  and  $\theta_r$  are the wind direction and the radar looking direction, respectively. (b) Sea surface observed along the radar beam.

**Table 3.** Settings of radar and conditions of wind and wave.

	Parameters	Notation	Value	Unit
Radar	Height from sea level	$H_r$	7.3	meter
	Direction to	$\theta_r$	310	degree
	Grazing angle	$\theta_g$	25	degree
	Transmission frequency	$f_T$	24	GHz
Wind	Direction from	$\theta_w$	319	degree
	Average speed	$U_{10}$	7.3	m/s
Wave	Significant wave height	$H_s$	0.24	meter
	Mean wave period	$T_z$	2.4	second

### 3.2. Data Processing

#### 3.2.1. Backscatters

The short-range K-band transceiver provides in-phase and quadrature outputs with two separate channels, which can be combined into a complex signal. Using the STFT, the complex signal is transformed into a series of spectra which can be used to produce a time-frequency-power spectrogram, as shown in Figure 6. The bright regions in the spectrogram represent the strong backscatters from the sea surface. The Bragg-scattering in the spectrogram was mostly originated from advancing Bragg waves propagating in wind direction. The Bragg-scattering originating from receding Bragg waves was too weak to be seen.

#### 3.2.2. DSF Extraction and Sea-spike Removal

A time series of DSF can be extracted by searching the maximum power for each instant of the spectrogram in Figure 6. However, a few strong points appear with roughly same power at the same instant so that we need to consider both the strongest points and the secondary points. A 20-point moving average is used to smooth the powers in the frequency space. The 20 points occupy 40 Hz which approximately equates to the standard deviation of the extracted DSF. The resultant spectrogram is shown in the upper part of Figure 7. The black line is the extracted DSF, in which each point is the frequency of the maximum power at different instant. The mean value of the extracted DSF is 112.4 Hz

which is much higher than  $f_{b\pm}$  (about  $\pm 15.8$  Hz) because the surface current and the Stokes drift carried the Bragg waves in the effective footprint towards the radar. Although the spikes are relatively strong, the number of spikes is small. Thus, their effect on the mean value is negligible.

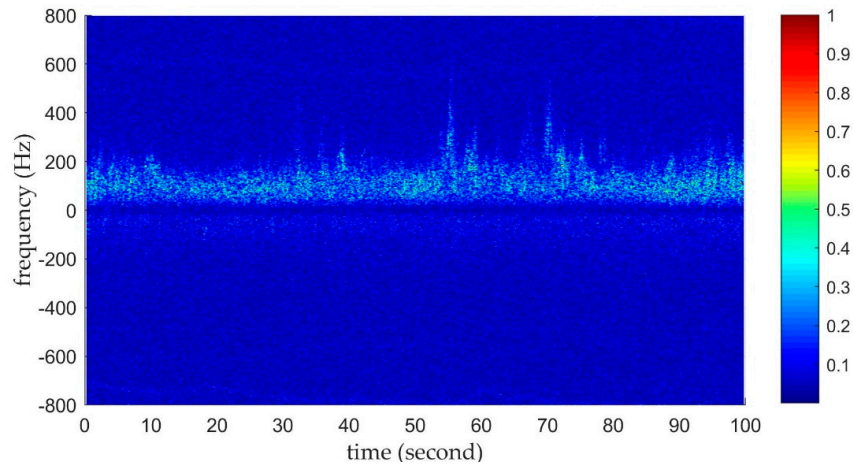


**Figure 6.** Normalized power spectrogram of a 100-s IF output. The sampling rate is 1600 Hz. The resolutions of time and frequency are 0.1 s and 2 Hz, respectively.

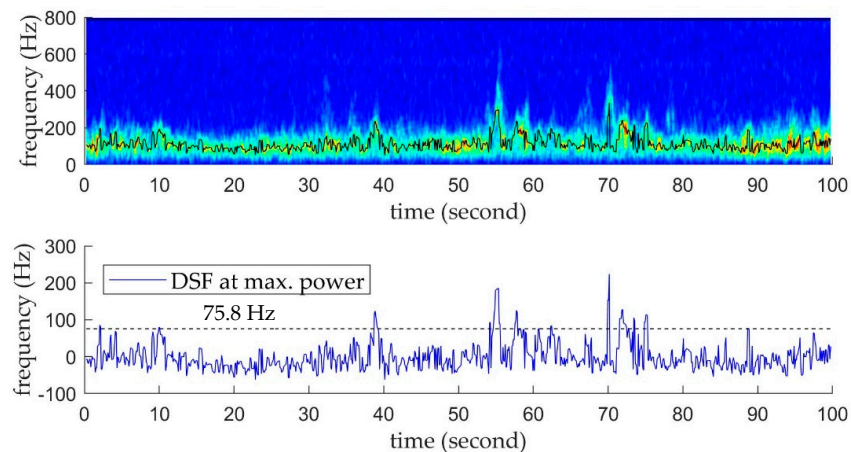


**Figure 7.** DSF extraction and sea spikes identification. 75.8 Hz equates to twice the standard deviation of the extracted DSF.

We cannot say that the extracted DSF is  $f_{\Sigma}$  because some high sea spikes appear with large frequency spreads. A threshold is used to identify the sea spikes, which equates to twice the standard deviation (37.9 Hz) of the extracted time series, 75.8 Hz. The lower portion of Figure 7 is the time series of extracted DSF and its mean value (112.4 Hz) is removed. The peaks exceeding the threshold are considered the sea spikes. The widths of all the sea spikes are less than 1 s. Therefore, a moving average is used to remove sea spikes because the identified sea spikes are so narrow that the trend of  $f_{\Sigma}$  at sea spikes can be predicted by the adjacent DSF. The moving average is only applied for the time period when the sea spikes occurred. The length of the moving average is set to 10 points, corresponding to 1 s.

The upper part of Figure 8 shows the comparison of the DSF before and after the sea spikes removal. The constant  $f_{b\pm}$  and  $f_c$  in  $f_{\Sigma}$  have been removed by subtracting mean value.  $f_p$  does not exist because the radar was on the stationary dock. After removing the sea spikes,  $f_d$  and  $f_w$  remain, as shown as the blue line in the upper part.  $f_d$  was caused by the Stokes drift speed. When some dominant wind waves came into the effective footprint, the Stokes drift carried water along the wave direction. When the waves moved out, the Stokes drift in the effective footprint disappeared. We use a

moving average to estimate the fluctuations of  $f_d$ . The mean spectral period is used as the time length of the moving average, but it is unknown. Here, the reciprocal of the mean value of the upper and lower limits of frequency range of wind wave is used:

$$T_a = \frac{1}{(f_{c1} + f_{c2})/2} \quad (13)$$

where  $f_{c1}$  is the lower limit, which is estimated as the separation frequency between wind wave and swell [26]:

$$f_{c1} = \frac{g}{2\pi U_{10}} \quad (14)$$

$f_{c1}$  is 0.21 Hz when  $U_{10}$  is 7.3 m/s.  $f_{c2}$  is 0.64 Hz which is the upper limit of frequency range of wave spectrum provided by wave buoy. Therefore,  $T_a$  is calculated to be 2.4 s. The green line in the upper part of Figure 8 is the result of the moving average,  $f_d$ .  $f_w$  can be derived by subtracting  $f_d$  from the DSF in which the sea spikes have been removed, (see the blue line in the upper part of Figure 8).  $f_w$  is shown in the lower part of Figure 8. Figure 9 shows the wave spectrum measured by the wave buoy. The vertical line at 0.21 Hz ( $f_{c1}$ ) separates the wind wave and swell components of the wave spectrum.

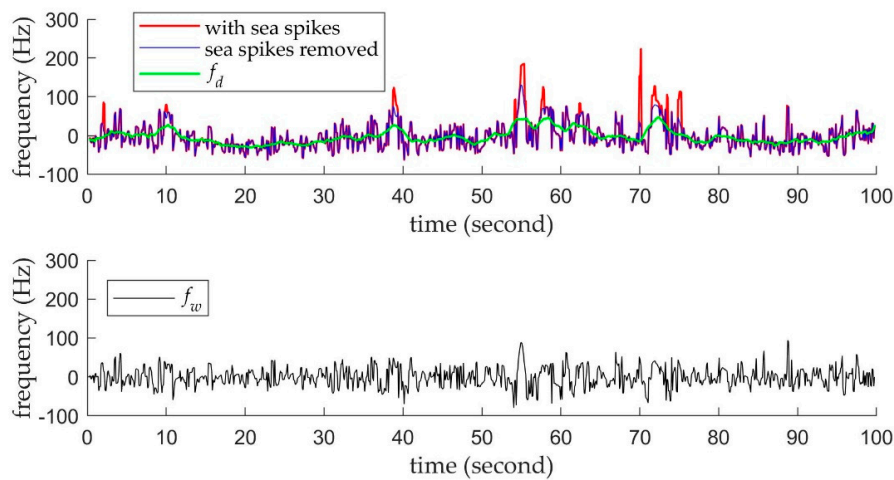


**Figure 8.** Sea spike removal using moving average and the removal of  $f_d$ .

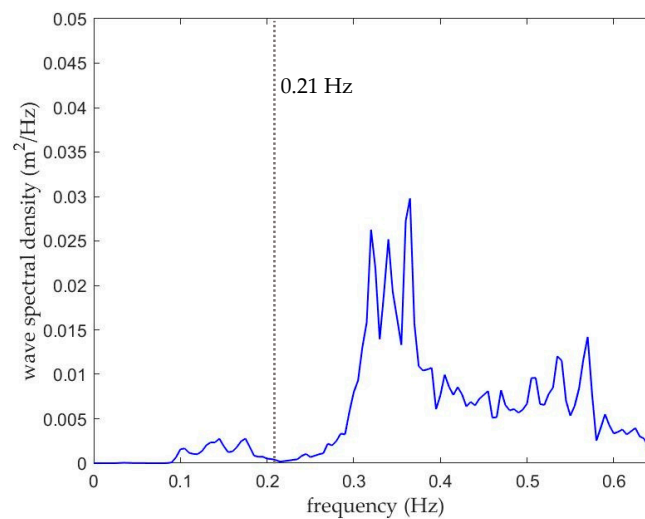


**Figure 9.** The wave spectrum measured with a TRIAXYS Wave Buoy. It was located at (Latitude: 47°27.708' N, Longitude: 53°6.498' W) and operated by Marine Institute of Memorial University of Newfoundland. More information is available at SmartAtlantic.ca.

### 3.2.3. Spectra and Characteristics of Wind Waves

The amplitude spectrum of the time series of  $f_w$  (see the black line in the lower part of Figure 8) is shown in Figure 10. Substituting the amplitude spectrum into Equation (8), the wave height spectrum is obtained.

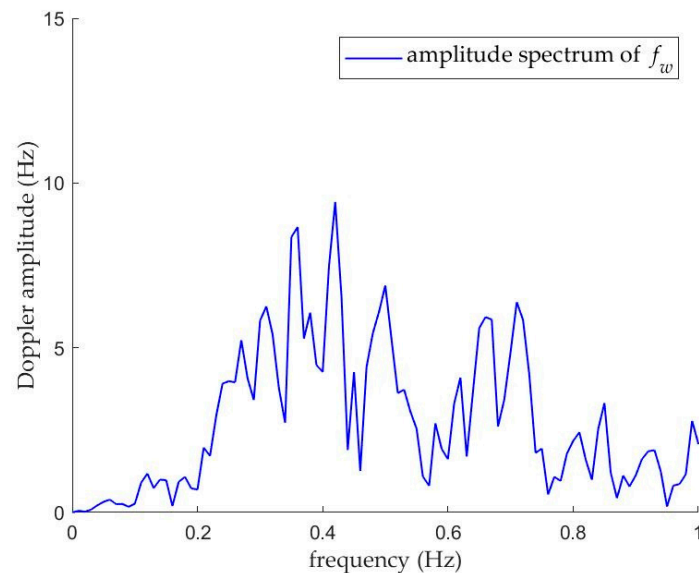


**Figure 10.** Amplitude spectrum of  $f_w$ .

The wind wave spectral density is calculated with Equation (9) and shown in Figure 11. The peaks greatly increase from the separation frequency, 0.21 Hz. It should be noted that the frequency range of the wave spectrum measured by buoy is from 0 Hz to 0.64 Hz, for better comparison between the radar and buoy, the higher frequency components in the radar-derived spectrum is truncated (see Figure 11). In fact, the spectral density of the components higher than 0.64 Hz is very low and negligible. The characteristics of the wind waves are calculated with Equations (10) and (11) and are tabulated in Table 4. It should be mentioned that same integration limits (0 Hz ~ 0.64 Hz) are used in Equation (12) for both radar- and buoy-measured spectra.

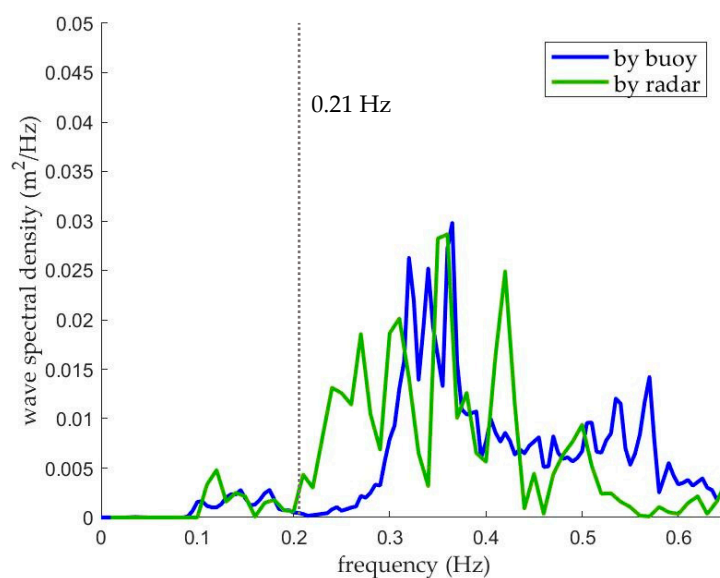


**Figure 11.** Wind wave spectra measured by buoy and radar.

**Table 4.** Characteristics of wind waves.

Device	$H_s$ (meter)	$T_z$ (second)
Buoy	0.24	2.4
Radar	0.25	1.9

## 4. Boat-Based Experiment

### 4.1. Conditions and Setup

The experiment was conducted to further validate the measurement of the wind wave spectra with the short-range K-band radar mounted on a small-sized boat (Narwhal inflatable craft). Figure 12a shows the experimental setup. The boat was equipped with the K-band radar, a GPS module, an attitude and heading reference system (AHRS), and a camera. All the sensors were arranged in the same vertical plane through the longitudinal centerline of the boat. The radar was about 2 meters above the sea surface. The radar transceiver was covered with a cylindrical radome, and pointed towards the sea surface with a 5-degree grazing angle; the GPS module logged the location and the ground speed of the boat; the AHRS measured the rotational motions and headings of the radar; the camera recorded images of the sea state. The location of the experiment was Holyrood Bay of Newfoundland, Canada, shown in Figure 12b. The red point indicates the location of the boat, and the two arrows depict the wind direction and radar looking direction, respectively.

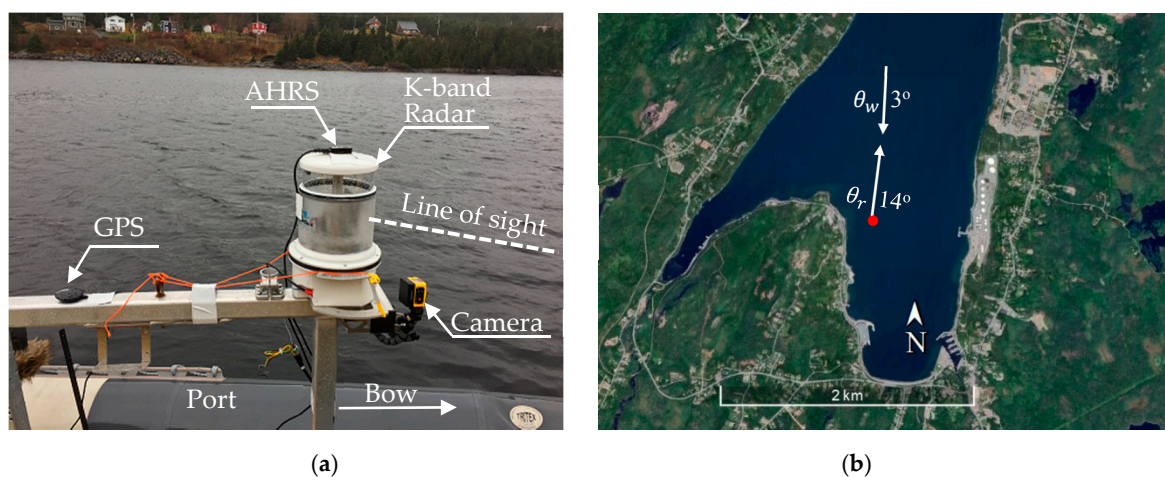


**Figure 12.** (a) Radar and auxiliary sensors on the boat. (b) Location of the experiment.

Table 5 includes the settings and conditions in the experiment. Figure 13 shows the sea state photo taken by the camera. The wind waves were propagating towards the boat and wave breaking was observed. A TRIAXYS Wave Buoy was deployed near the boat. As the dock-based experiment, the wind sensor measured the wind direction and the average wind speed  $U_2$ , which was converted to  $U_{10}$ .

### 4.2. Data Processing

#### 4.2.1. Backscatters

All the sensors operated synchronously. As the data processing for the dock-based experiment, the output IF signals of the short-range K-band transceiver (K-MC3) are transformed into a time-frequency-power spectrogram (see Figure 14) with the method of STFT. The strong backscatters is much higher than  $f_{b\pm}$  (about  $\pm 15.8$  Hz), a shift that is likely a result of the boat motions. However, there was no shift from the surface current that moved both the sea water in the effective footprint and

the boat at the same velocity. Most of the Bragg-scattering originated from the advancing Bragg waves propagating in wind direction, while the Bragg-scattering originated from receding Bragg waves was too weak to be seen in the spectrogram. The noise in the background was due to electromagnetic interference from the device on the boat.

**Table 5.** Settings of radar and conditions of wind, wave, and boat.

	Parameters	Notation	Value	Unit
Radar	Height from sea level	$H_r$	2	meter
	Direction to	$\theta_r$	14	degree
	Grazing angle	$\theta_g$	5	degree
	Transmission frequency	$f_T$	24	GHz
Wind	Direction from	$\theta_w$	3	degree
	Average speed	$U_{10}$	8.4	m/s
Wave	Significant wave height	$H_s$	0.41	meter
	Mean wave period	$T_z$	2.7	second
Boat	Ground speed	$U_b$	0.53	m/s



**Figure 13.** Sea surface observed at the bow of the boat. Some raindrops partially obscured the camera lens.

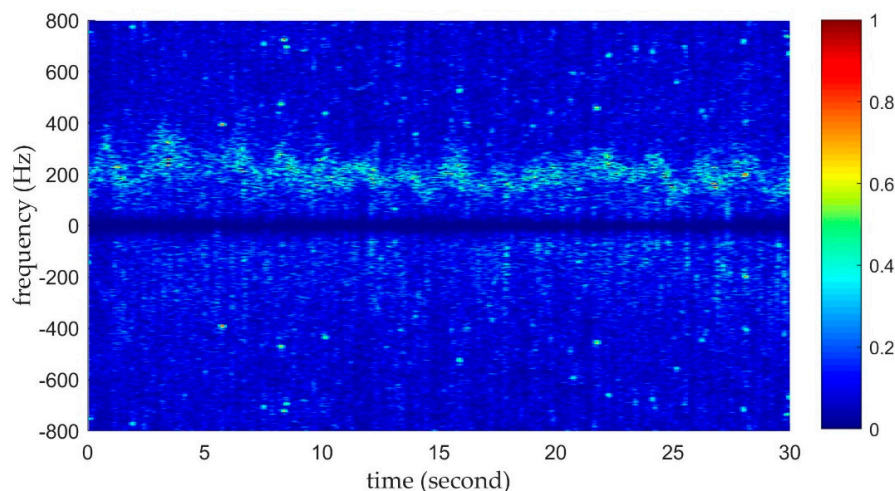


**Figure 14.** Normalized power spectrogram of a 30-s IF output of the K-band radar. The sampling rate is 1600 Hz. The resolutions of time and frequency are 0.1 s and 2 Hz, respectively.

#### 4.2.2. DSF Extraction and Motion Compensation

Before extracting the DSF from the spectrogram shown in Figure 14, the spectrogram is processed in the same way as the dock-based experiment. An 18-point moving average is used to smooth the powers in the frequency space. The 18 points occupy 36 Hz which is approximately equal to the standard deviation of the extracted DSF. The processed spectrogram is shown in the upper part of Figure 15. The black line is the time series of DSF extracted by searching the maximum power for each instant in the processed spectrogram. The mean value of the extracted DSF is 201.3 Hz which is mainly due to the boat motions. The lower part of Figure 15 shows the extracted DSF in which the low fluctuations and the mean value have been removed for sea spike identification. A value of twice the standard deviation is used as a threshold to identify the sea spikes. There are not many sea spikes and the widths are less than 0.5 s. Similarly, the moving average is used to remove the sea spikes and the length of the moving average is set to 5 points, corresponding to 0.5 s.

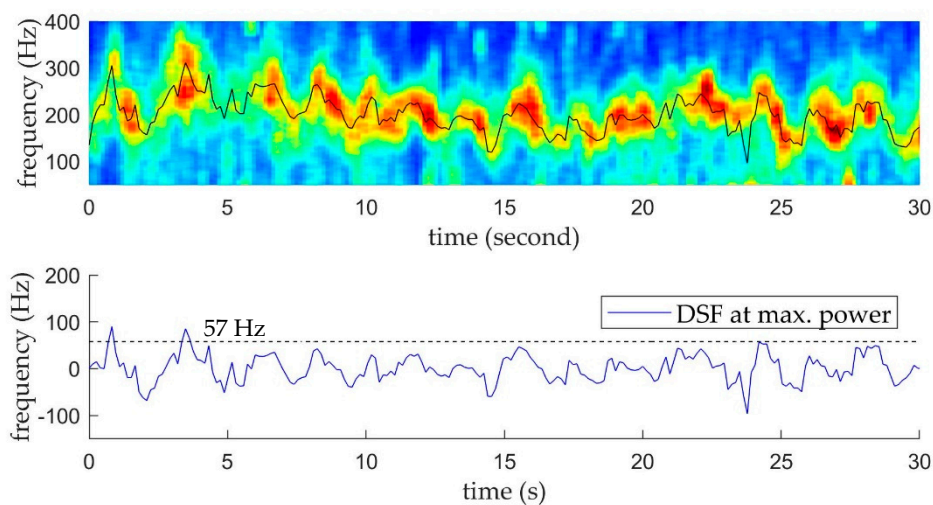


**Figure 15.** DSF extraction from the processed spectrogram and sea spikes identification.

The rotational motions of the radar were compensated with a closed loop control process. The orientation of the radar's transceiver was measured with the AHRS and sent to a controller which operated a stepper motor and a linear actuator to keep the direction and the grazing angle of the radar transceiver unchanged during the measurement. However, there was a constant drifting in the heading measurement. It drifted 7 degrees in 30 s, which is equal to the azimuthal beam width of the radar. We only used the 30-s radar data of the boat-based experiment, because 7-degree drifting made the effective footprint completely deviate from the directions that the footprint covered at the beginning of the 30 s. On the other hand, the linear motions of the radar were recorded, and the location of the effective footprint was also estimated according to the height and the grazing angle of the radar. Therefore, the radar's velocity relative to the center of the effective footprint is calculated and then the DSF  $f_p$  is determined, as shown with the red curve in Figure 16. The blue curve is the extracted DSF in which the sea spikes have been removed. The black curve represents the difference between the two curves, which is considered as the DSF  $f_w$ . The difference does not include DSF  $f_d$  because the boat was close to the effective footprint so that Stokes drift not only moved the sea water in the effective footprint but also moved the boat. The mean value of the  $f_w$  differs from 0 Hz because of the measurement error of the boat ground speed, which results in the low frequency components in the time series of DSF  $f_w$  (see the black line).

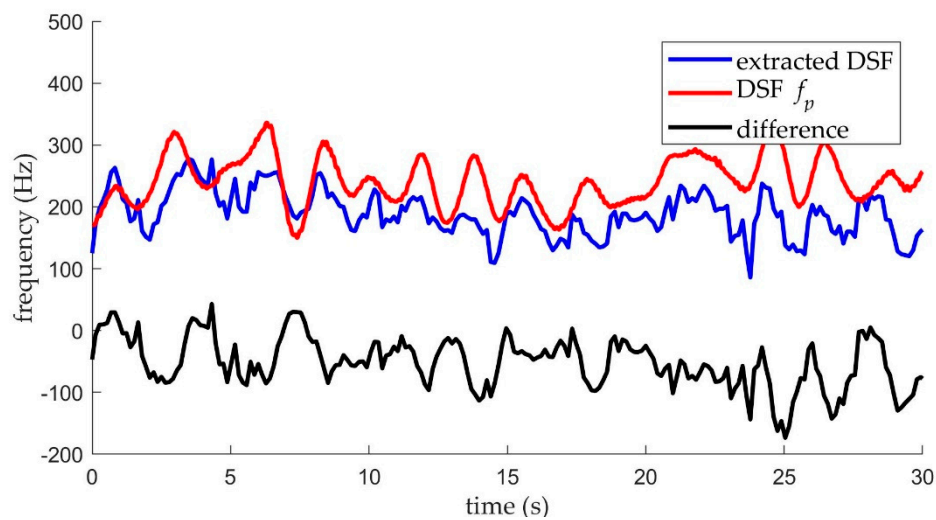


Figure 16. Removal of DSF  $f_p$ .

#### 4.2.3. Spectra and Characteristics of Wind Waves

The time series of  $f_w$  is transformed into an amplitude spectrum, as shown in Figure 17. The peaks on the right of the separation frequency (0.18 Hz) were caused by wind waves, the peaks on the left side were due to the measurement error of the boat ground speed. The spectrum of wind waves is obtained with Equations (8) and (9) and shown in Figure 18. The characteristics of the wind waves are calculated from Equations (10) and (11) and are tabulated in Table 6.

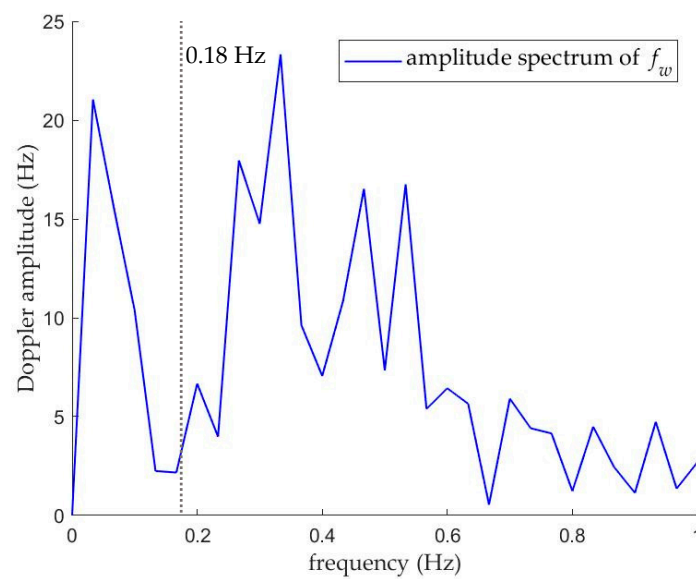


Figure 17. Amplitude spectrum of  $f_w$ .

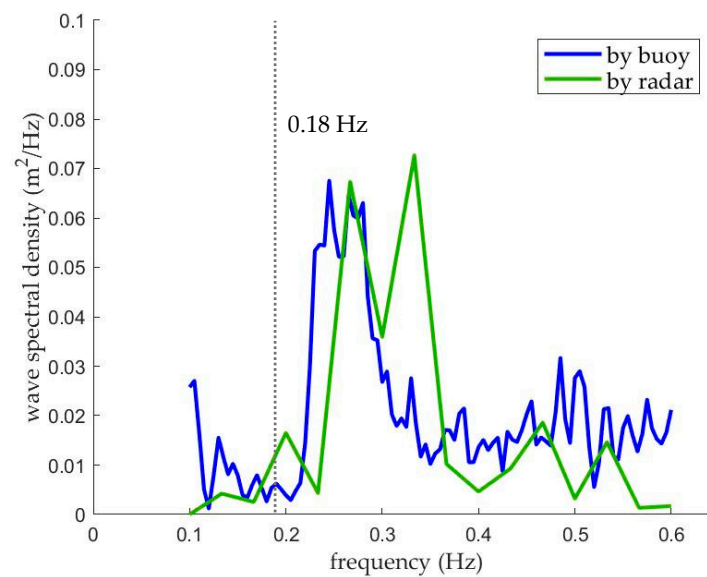


Figure 18. Wind wave spectra measured by buoy and radar.

Table 6. Characteristics of wind waves.

Device	$H_s$ (meter)	$T_z$ (second)
Buoy	0.41	2.7
Radar	0.38	2.9

## 5. Discussion

We carried out two experiments at sea to measure the spectra of wind waves using a short-range K-band radar. The wind waves generated by local winds dominated. The radar was set to point in the direction of the wind and the wind waves during the testing. Therefore, the measured spectrum primarily illustrates the wind waves.

The size of the effective footprint is a key factor in considering the wavelengths measured by the radar. The measurement with a relatively small effective footprint enables the detection and identification of short wind waves with high resolution. In Figures 11 and 18, the measured spectra by the radar drastically decrease from the right side of 0.4 Hz. It implies that the effective footprint in the experiments cannot identify short wind waves oscillating faster than 0.4 Hz. Therefore, we need to adjust the radar height and the grazing angle to achieve a small effective footprint, or use other K-band transceiver that features narrower beam widths than the current one.

Some factors cause errors in the measurement of the wave characteristics, as seen in Tables 4 and 6. First, the measurement durations (100 s and 30 s) were short so some components of the wind wave spectrum were not fully observed. The short durations also cause low resolution in frequency of the wave spectra. Second, the sea spikes impact the extractions of the DSF. Even if the sea spikes are identified and removed, the DSF values cannot be completely retrieved by a moving average. Refracted wave will also affect the measurement accuracy although we noticed little evidence of wave refraction. The possible solutions to the error sources are to extend measurement durations, improve the method of sea spikes removal, and measure wave directions.

Comparing Figures 7 and 15, despite the higher wind speed in the boat-based experiment, the occurrence of sea spikes is much less than the dock-based experiment. The lower grazing angle contributes to the sea spike suppression. Less sea spikes result in more precise measurements.

## 6. Conclusions

The work presented in this paper supports the feasibility of using the short-range K-band radar for measurement of the non-directional wind wave spectrum at sea surface. The concept of the effective footprint is established, which is the basis of the technique. By adjusting the grazing angle according to the radar height over sea surface, the narrow beam illuminates an area in which sea water not only oscillates with the wind waves but also generates strong Bragg-scattering back to the radar. The motions of sea surface within the effective footprint cause the DSF in the backscattered signals. The sources of the DSF components are analyzed. The Bragg waves lead to a constant DSF component determined by the radar wavelength and the grazing angle. The surface current also causes a constant DSF component proportional to the current velocity. The Stokes drift also contributes to the DSF fluctuations. Platform motion causes a relative velocity between the radar and the effective footprint, which is another source of DSF. The former two constant components can be removed by subtracting the mean of the DSF; the latter two unpredictable components can be calculated with a moving average and three linear motions of the radar, and removed from the total DSF. The remaining components originate from the surface gravity waves and can be transformed from a time series of DSF into a wave spectrum. The processing flow for the radar output is given and performed for the two experiments.

The two experiments were carried out to measure the wind waves from a dock and a boat. In the dock-based experiment, the breaking waves caused some sea spikes in the DSF, and they needed to be identified and removed before any further processing. Twice the standard deviation of the time series of extracted DSF is used as a threshold to identify the sea spikes. The identified sea spikes are removed by predicting DSF values with moving average over the sea spikes. The DSF caused by Stokes drift is estimated by moving average, and the length of the moving average equates to the reciprocal of the mean value of the upper and lower limits of frequency range of wind waves. In the boat-based experiment, three rotational motions of the radar were mechanically compensated, while three linear motions caused a heavy component of DSF which was proportional to the radar's velocity relative to the effective footprint. The sea spikes and the constant DSF components can be removed as the processing in the dock-based experiment. The DSF components of the linear motions can be directly subtracted from the resultant time series of DSF. The remaining time series of DSF in the two experiments are transformed into the spectra of the wind waves which are approximate to the spectra measured by the wave buoys.

Future work should include the measurement of swell and long period gravity waves using the same radar. The direction factors of the spectra of swell and long period gravity waves will be measured with multi-transceivers radar that can sense the surface motions in different directions simultaneously. In the future, it would also be worth investigating the detection of refracted waves and small variations of wave direction.

**Author Contributions:** J.C. performed the experiments and drafted the manuscript. R.B., B.d.Y. and W.H. supervised the study, and contributed to the design of the experiments and the interpretation of the results. All the authors contributed to the editing of the manuscript.

**Funding:** This research was undertaken as part of the Ice Ocean Sentinel System (IOSS) project, funded by the Canadian Atlantic Innovation Fund (#781-2636-201155) the Research and Development Corporation Newfoundland, the Province of Newfoundland, and the Terra Nova Project.

**Acknowledgments:** The research is part of the research of the unmanned surface craft program funded by Ice Ocean Sentinel System, Atlantic Canada Opportunities Agency—Atlantic Innovation Fund. The authors appreciate the assistance and support of Neil Riggs, Haibing Wang, and Federico Luchino during the development of the short-range K-band and the wave tank experiments.

**Conflicts of Interest:** The authors declare no conflict of interest.

## Abbreviations

The following abbreviations are used in this manuscript:

AHRS	Attitude and Heading Reference System
CW	Continuous Wave
DSF	Doppler Shift Frequency
FMCW	Frequency Modulated Continuous Wave
IF	Intermediate Frequency
SAR	Synthetic Aperture Radar
STFT	Short Time Fourier transform

## References

1. Radac's X-Band WaveGuide, RADAC B.V. Available online: <https://radac.nl/wave-height-tide/> (accessed on 5 July 2019).
2. Miros' C-Band WaveFinder, Miros AS. Available online: <https://www.miros-group.com/products/wavefinder/> (accessed on 5 July 2019).
3. Hilmer, T.; Thornhill, E. Deterministic wave predictions from the WaMoS II. In Proceedings of the OCEANS 2014–Taipei, Taipei, Taiwan, 7–10 April 2014. [CrossRef]
4. Trizna, B.D. Coherent marine radar measurements of ocean surface currents and directional wave spectra. In Proceedings of the OCEANS 2011 IEEE–Spain, Santander, Spain, 6–9 June 2011. [CrossRef]
5. Walsh, J.E.; Uliana, E.A.; Yaplee, S.B. Ocean wave heights measured by a high resolution pulse-limited radar altimeter. *Bound. Layer Meteorol.* **1978**, *13*, 263–276. [CrossRef]
6. Abdalla, S. Active techniques for wind and wave observations: Radar altimeter. In Proceedings of the Seminar on Use of Satellite Observations in Numerical Weather Prediction, Reading, UK, 8–12 September 2014.
7. Marom, M.; Goldstein, M.R.; Thornton, B.E.; Shemer, L. Remote sensing of ocean wave spectra by interferometric synthetic aperture radar. *Nature* **1990**, *345*, 793–795. [CrossRef]
8. Sui, X.; Zhang, R.; Wu, F.; Li, Y.; Wan, X. Sea surface height measuring using InSAR altimeter. *Geod. Geodyn.* **2017**, *8*, 278–284. [CrossRef]
9. Cui, J.; Bachmayer, R.; deYoung, B.; Huang, W. Retrieval of ocean wave characteristics from K-band radar. In Proceedings of the OCEANS 2016 MTS/IEEE, Monterey, CA, USA, 19–23 September 2016. [CrossRef]
10. Cui, J.; Bachmayer, R.; deYoung, B.; Huang, W. Motion compensation of K-band radar ocean wave measurement. In Proceedings of the OCEANS 2017, Aberdeen, UK, 19–22 June 2017. [CrossRef]
11. Cui, J.; Bachmayer, R.; deYoung, B.; Huang, W. Ocean wave measurement using short-range K-band narrow beam continuous wave radar. *Remote Sens.* **2018**, *10*, 1242. [CrossRef]
12. Steele, H.J.; Thorpe, A.S.; Turekian, K.K. *Elements of Physical Oceanography: A Derivative of the Encyclopedia of Ocean Sciences*; Academic Press: Cambridge, MA, USA, 2009; p. 290, ISBN 0123757215.
13. Phillips, O. Radar return from the sea surface—Bragg scattering and breaking waves. *J. Phys. Oceanogr.* **1998**, *18*, 1065–1074. [CrossRef]
14. Poulter, M.E.; Smith, J.M.; McGregor, A.J. Microwave backscatter from the sea surface: Bragg scattering by short gravity waves. *J. Geophys. Res.* **1994**, *99*, 7929–7943. [CrossRef]
15. Kundu, K.P.; Cohen, M.I.; Dowling, R.D. *Fluid Mechanics*; Academic Press: Cambridge, MA, USA, 2015; pp. 382–383, ISBN 0124071511.
16. Sorensen, M.R. *Basic Wave Mechanics: For Coastal and Ocean Engineers*; John Wiley & Sons: New York, NY, USA, 1993; pp. 14–17, ISBN 978-0471551652.
17. Carrasco, R.; Horstmann, J.; Seemann, J. Significant wave height measured by coherent X-band radar. *IEEE Trans. Geosci. Remote Sens.* **2017**, *55*, 5355–5365. [CrossRef]
18. Rosenberg, L. Sea-spike detection in high grazing angle X-band sea-clutter. *IEEE Trans. Geosci. Remote Sens.* **2013**, *51*, 4556–4562. [CrossRef]
19. Greco, M.; Stinco, P.; Gini, F. Identification and analysis of sea radar clutter spikes. *IET Radar Sonar Navig.* **2010**, *4*, 239–250. [CrossRef]
20. Kingsley, S.; Quegan, S. *Understanding Radar Systems*; Electromagnetics and Radar Radar, Sonar, Navigation and Avionics; SciTech Publishing: Raleigh, NC, USA, 1999; Volume 2, pp. 226–230, ISBN 1891121057.

21. Sawaragi, T. *Coastal Engineering—Waves, Beaches, Wave-Structure Interactions*; Developments in Geotechnical Engineering; Elsevier: Amsterdam, The Netherlands, 1995; Volume 78, pp. 7–11, ISBN 978-0-444-82068-6.
22. Gudmestad, O. *Marine Technology and Operations: Theory and Practice*; WIT Press: Chilworth, Southampton, UK, 2015; p. 289, ISBN 1784660388.
23. Tan, L.; Jiang, J. *Digital Signal Processing: Fundamentals and Applications*; Academic Press: Cambridge, MA, USA, 2018; pp. 102–112, ISBN 0128150726.
24. Pecher, A.; Kofoed, P.J. *Handbook of Ocean Wave Energy*; Ocean Engineering & Oceanography; Springer: Berlin, Germany, 2016; Volume 7, pp. 57–60, ISBN 331939889X.
25. Holmes, D.J. *Wind Loading of Structures*; CRC Press: Boca Raton, FL, USA, 2007; pp. 56–60, ISBN 0203964284.
26. Wang, W.D.; Hwang, A.P. An operational method for separating wind sea and swell from ocean wave spectra. *J. Atmos. Ocean. Technol.* **2001**, *18*, 2052–2062. [[CrossRef](#)]



© 2019 by the authors. Licensee MDPI, Basel, Switzerland. This article is an open access article distributed under the terms and conditions of the Creative Commons Attribution (CC BY) license (<http://creativecommons.org/licenses/by/4.0/>).